ARTICLE

Self-Organization of Te Nanorods into V-Shaped Assemblies: A Brownian Dynamics Study and Experimental Insights

Sachin Shanbhag,[†,‡] Zhiyong Tang,[§] and Nicholas A. Kotov[⊥,∥,#,*]

[†]Department of Chemical and Biomedical Engineering, FAMU–FSU College of Engineering, Tallahassee, Florida 32310, [‡]School of Computational Science, Florida State University, Tallahassee, Florida 32306, [§]National Center for Nanoscience and Technology, Beijing 100080, China, and [⊥]Departments of Chemical Engineering, [∥]Materials Science and Engineering, and [#]Biomedical Engineering, University of Michigan, Ann Arbor, Michigan 48109

ABSTRACT Computer modeling of nanoscale processes provides critical quantitative insights into nanoscale self-organization, which is hard to achieve by other means. Starting from a suspension of Te nanorods, it was recently found that short nanorods (50 nm) self-organized into checkmark-like V-shaped assemblies over a period of a few days, whereas long nanorods (2200 nm) did not. This experimental fact was difficult to explain, and so here we use Brownian dynamics simulations of a dilute suspension of hard spherocylinders to better understand the process of self-organization. With the assumption that close encounters between nanorod tips result in their merger into V-particles, it was found that the ratio of the initial rate of nanorod formation for the short and long rods was 3760. By systematically varying the length and the concentration, we found that the concentration of the nanorods, rather their length, was primarily instrumental in setting the initial rate of checkmark formation. Using a simple kinetic model in conjunction with experimental data, we find that approximately 30 000 close encounters are required on average for a single successful merger. This study gives an important reference point for understanding the mechanism of the formation of complex nanostructured system by oriented attachment; it also can be extended to and provides conceptual leads for other self-organized systems.

KEYWORDS: Te nanorods · V-particles · Brownian dynamics · self-assembly · oriented attachment · nanoscale assemblies

*Address correspondence to kotov@umich.edu.

Received for review July 6, 2007 and accepted August 30, 2007.

Published online September 28, 2007. 10.1021/nn7000905 CCC: $37.00

A variety of regular non-spherical nanocolloids have been synthesized, such as wires, tubes, disks, and more exotic structures such as prisms and branched structures.[1–10] These nanocolloids have been prepared from materials such as CdS, CdSe, CdTe, PbS, PbSe, ZnSe, MnS, TiO_2, Au, *etc.*[11–21] through a number of synthetic routes. While there is a lot of excitement in the scientific community about the chemical, optical, and electronic properties of such quantum-confined structures, governed by their chemical composition, size, and shape, many unanswered questions remain about the mechanisms of formation of such complex nanoscale systems. Only for tetrapods[9,13] and systems formed by oriented attachment[14,15,19,22–28] have more-detailed pictures of the assembly mechanisms been suggested. Computer modeling of nanoscale self-organization processes[29–31] can provide a critical link between the experimental observations and proposed theoretical understanding of these mechanisms,[32–34] which can be particularly obscure for particle assemblies involving chemical processes at the interface. Computer modeling also makes possible quantitative evaluation of the parameters necessary for self-organization.

Recently,[35] we reported the synthesis of highly angled, asymmetrically branched Te nanocrystals (see inset in Figure 1). These nanoscale V-particles, resembling checkmarks, were formed when the L-cysteine stabilizer shell on water-soluble CdTe nanoparticles was partially removed in the presence of ethylenediaminetetraacetic acid to form Te nanorods. It was found that, starting from short Te nanorods (50 nm), a large

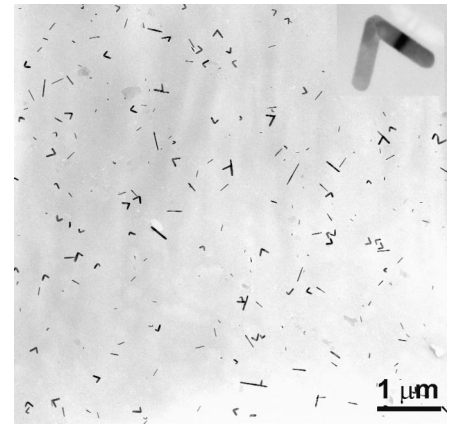

Figure 1. Scanning electron micrograph (SEM) of a nanorod suspension showing the presence of V-particles. The inset shows a close-up of a nanoscale checkmark.

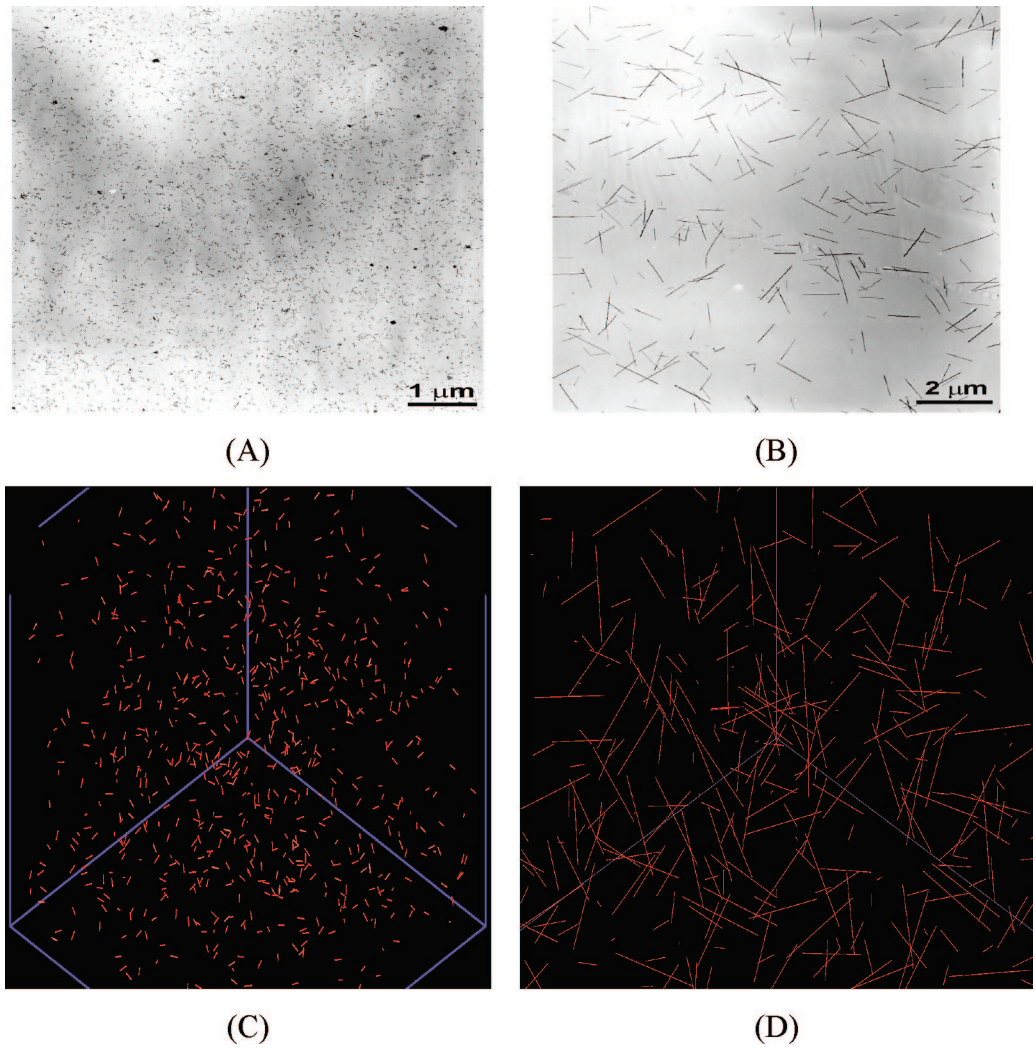

Figure 2. SEM images of (A) short and (B) long nanorods. The short and long rods have size distributions of L = 12–80 nm and L = 400–4000 nm, respectively. Snapshots corresponding to monodisperse model systems with (C) L = 46 nm and (D) L = 2200 nm are also shown.

number of nanoscale checkmarks were formed that evolved into moth-like shapes over a period of a few days. However, starting from long Te nanorods (2200 nm), angled structures were not observed. Unlike other synthetic routes for building branched nanostructures, V-particles arise due to collisions of individual nanorods followed by oriented attachment[14,15,19,22–28] along a (201) or (102) surface of the Te crystal lattice.[35] This system provides exemplary testing grounds for computer modeling of the self-organization processes involving interfacial chemical reactions between particles using fairly standard methods of molecular simulations.

In this work, we use Brownian dynamics (BD) simulations to model the incidence of V-particle formation and to attempt to explain experimental observations. We found that the rate of V-assembly for the short rods was 3 orders of magnitude larger than that for long rods. We explored the relative contributions of length and concentration and found that it is the concentration of the nanorods that largely governs the initial rate of V-particle formation. By comparing calculations with experimental data, we surmised that approximately 30 000 close encounters are required on average for a single successful merger of the short nanorods into a nanoscale checkmarks. Typically, the self-assembly of nanoscale building blocks into more complex structures is carried out in solution at a relatively low concentration due to the lower transport barriers. This model and the methods developed here can be applied to a variety of other processes of self-organization of nanoscale colloids.

RESULTS AND DISCUSSION

a. Simulation System. In the experimental system reported, nanoscale checkmarks, or "V-particles", were observed for short nanorods (Figure 1), where the length and diameter of the nanorods varied over the ranges L = 12–80 nm and b = 7–9 nm, respectively.[35] For the long nanorods (Figure 2B), the length and diameter varied over L = 400–4000 nm and b = 16–18 nm, respectively. The concentration of the precursor solution, $c_{precursor}$, was 8.836 mM. The volume of an individual Te spherocylinder is calculated as

$$V = \frac{\pi b^3}{4}\left[\frac{L}{b} + \frac{2}{3}\right] \quad (1)$$

In this study, we ignored the polydispersity and assumed a monodisperse sample of $L = 46$ nm and $b = 8$ nm for the short rods, corresponding to the average length and diameter found in the polydisperse experimental sample. Similarly, we assumed $L = 2200$ nm and $b = 17$ nm for the long nanorods. The concentration of the nanorods can be computed from stoichiometry and eq1 as $c = \rho_{Te} V N_A / M_{Te}$, where $\rho_{Te} = 6.24$ g/cm^3 and $M_{Te} = 127.6$ Da are respectively the bulk density and molecular weight of Te, and $N_A = 6.022 \times 10^{23}$ is Avogadro's constant. The volume of the simulation system was chosen to ensure that about 1000 rods were represented in each simulation box. Therefore, the range of V was approximately 10–3000 μm^3. Thus, the concentrations of the short and long rods are $c(L=46) = 1.3 \times 10^{-7}$ M and $c(L=2200) = 6.01 \times 10^{-10}$ M, corresponding to number densities $\nu(L=46) = 7.83 \times 10^{-8}$ rods/nm^3 and $\nu(L=2200) = 3.62 \times 10^{-10}$ rods/nm^3. For short rods, $\nu < 1/L^3$, which implies that the solution is dilute.[38] For the long rods, $1/L^3 < \nu < 1/bL^2$, which indicates that the solution is semidilute and there is interference in the rotational and translational motions of these nanorods (see Figure 2).

b. Comparison with Experiment. Figure 3 depicts the number of close encounters per milliliter of nanoparticle suspension, $N_{ce}(r^*)$, for $L = 46$ nm and $L = 2200$ nm as r^*, the radius of the sphere of interaction (SOI; see Figure 4), is varied. At a given r^*, $N_{ce}(r^*)$ for the short rods is more than 3 orders of magnitude larger than $N_{ce}(r^*)$ for the long rods. As expected, $N_{ce}(r^*)$ increases as the radius of the SOI r^* increases, since there is greater chance for a neighboring nanorod to pervade a larger unit of volume. We observe that the ratio $N_{ce}(L=46)/N_{ce}(L=2200)$ varies weakly with r^*, increasing from about 4330 to 5010 as r^* increases from $2b$ to $4b$. The large magnitude of this ratio explains why the occurrence of nanocheckmarks is observed far more frequently in short rods ($L = 46$ nm) than in long rods ($L = 2200$ nm).

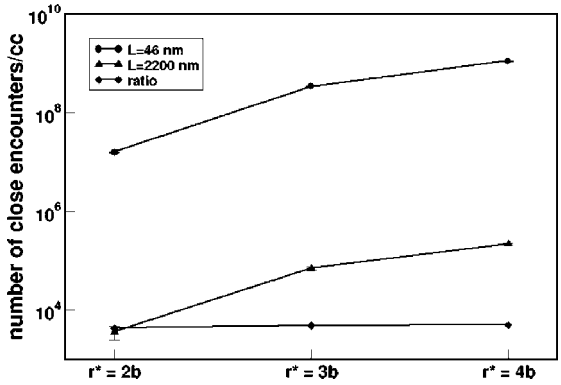

Figure 3. Average number of close encounters per milliliter of nanorod suspension, N_{ce}, as a function of the radius of the sphere of interaction, r^*. N_{ce} for the short rods (●) is more than 3 orders of magnitude greater than N_{ce} for $L = 2200$ nm (▲). The ratio of the $N_{ce}(r^*)$ values for $L = 46$ nm and $L = 2200$ nm is relatively constant at 3760.

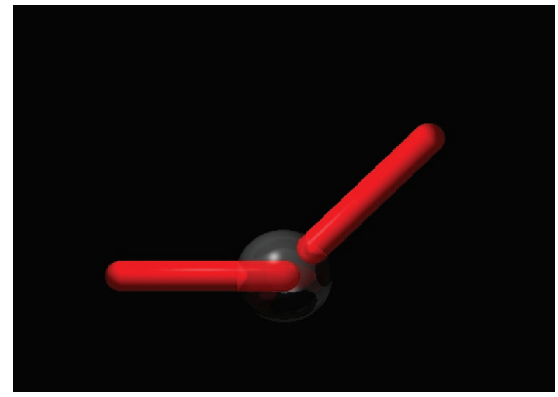

Figure 4. A sphere of interaction (SOI), represented by the transparent sphere, centered on one end of a terminal sphere of a spherocylindrical nanorod. Here, the radius r^* of the SOI is $2b$, where b is the diameter of the nanorod. A close encounter occurs when the end of an approaching nanorod enters this SOI.

It is likely that the formation of V-particles from short rods is further enhanced due to their mobility. Using a simple scaling relationship for diffusivity of rigid rods, the ratio of the diffusivities of the short and long rods is[43]

$$\frac{D_s}{D_l} \approx \frac{\ln(L_s/b_s)}{\ln(L_l/b_l)}\left(\frac{L_l}{L_s}\right) = 17.20 \quad (2)$$

This additional mobility is perhaps instrumental in orchestrating the approach of nanorods so that energetically unfavorable (102) crystal faces are brought together. If we employ a naïve scaling argument for the frequency of collisions, $f \sim c^2$, which is strictly valid only for dilute spherical colloidal suspensions, then one obtains $(f_s/f_l) = (c_s/c_l)^2 \approx 46\,800$, which is an order of magnitude larger than the value obtained from simulation.

Further, we monitored the relative orientation of the nanorods as they approach each other. To quantify the relative orientation, we employed the order parameter,

$$S = 1.5\langle\cos^2\theta\rangle - 0.5 \quad (3)$$

where θ is the angle between the axes of the two nanorods. Thus, $S = 1$ when the rods are parallel to each other and perfectly aligned. When $S = 0$, the distribution is isotropic and there is no correlation between nanorod orientations. In eq 3, for a given r^*, the ensemble average, $\langle * \rangle$, runs over pairs of nanorods, i and j, whose tips are separated by a distance $d^*(i,j) < r^*$. The results for the short and long nanorods are tabulated in Table 1.

For both short and long rods, there appears to be a strong pressure to align as their tips approach other, largely due to steric factors. The orientational correlation between approaching rods decays with r^*, and

TABLE 1. Order Parameter S as a Function of r^* for the Experimental Systems Depicted in Figure 2

	L = 46 nm	L = 2200 nm
$r^* = 2b$	0.58 ± 0.01	0.68 ± 0.05
$r^* = 3b$	0.06 ± 0.00	0.08 ± 0.03
$r^* = 4b$	0.03 ± 0.00	0.01 ± 0.02

when $r^* = 4b$, the rod orientations appear to be almost isotropic.

c. Effects of Concentration and Length. In order to study the effects of concentration and length on the number of close encounters between nanorods, we considered two cases, as shown in Table 2. The diameter of the rod was held fixed at b =10 nm, and for each case the length of the rod was varied between 50 and 1000 nm. For Case (I), the concentration of the rods was held fixed at 10^{-8} M. This was to isolate the effect of the length of the nanorod. The total volume fraction of a nanorod suspension, ϕ, is equal to νV, where V is the volume of a nanorod, given by eq 1. For Case (II), φ was held constant and the concentration of the nanorods was varied according to the expression $c(L) = (50/L) \times 10^{-8}$ M. This corresponds to a fixed precursor solution concentration, similar to the experimental system mentioned previously.

For L = 1000 nm in Case(I), $1/L^3 < \nu > 1/bL^2$, and these suspensions are semidilute (see Table 2). All the other systems considered in Table 2 are dilute, since $\nu < 1/L^3$. The static properties of semidilute solutions are almost identical to those of dilute solutions, although molecular rotations are restricted. $N_{ce}(r^*)$ for the different cases is shown in Figure 5 as a function of the length of the nanorods. For Case (I), N_{ce} is independent of the length of the nanorod and is equal to 0.186×10^6, 3.92×10^6, and 12.78×10^6 cm^{-3} for $r^* = 2b$, $3b$, and $4b$, respectively. In dilute and semidilute solutions of relatively small suspension concentration ($\nu \ll 1/bL^2$), the distribution of nanorod tips is approximately uniform throughout the simulation volume and is independent of the length of the nanorod. Consequently, at a given

TABLE 2. Effects of Concentration and Length on the Number of Close Encounters between Nanorods[a]

L (nm)	C (nM)	$1/L^3$ (nm^{-3})	$1/bL^2$ (nm^{-3})	ν (rods/nm^3)	φ
			Case (I)		
50	10	8.00×10^{-6}	4.00×10^{-5}	6.02×10^{-9}	2.68×10^{-5}
100	10	1.00×10^{-6}	1.00×10^{-5}	6.02×10^{-9}	5.05×10^{-5}
250	10	6.40×10^{-8}	1.60×10^{-6}	6.02×10^{-9}	1.21×10^{-4}
500	10	8.00×10^{-9}	4.00×10^{-7}	6.02×10^{-9}	2.40×10^{-4}
1000	10	1.00×10^{-9}	1.00×10^{-7}	6.02×10^{-9}	4.76×10^{-4}
			Case (II)		
100	5	1.00×10^{-6}	1.00×10^{-5}	3.01×10^{-9}	2.68×10^{-5}
250	2	6.40×10^{-8}	1.60×10^{-6}	1.20×10^{-9}	2.68×10^{-5}
500	1	8.00×10^{-9}	4.00×10^{-7}	6.02×10^{-10}	2.68×10^{-5}
1000	0.5	1.00×10^{-9}	1.00×10^{-7}	3.01×10^{-10}	2.68×10^{-5}

[a] In Case (I), the concentration is held fixed, while in Case (II), which corresponds to a fixed concentration of precursor solution, φ is held fixed.

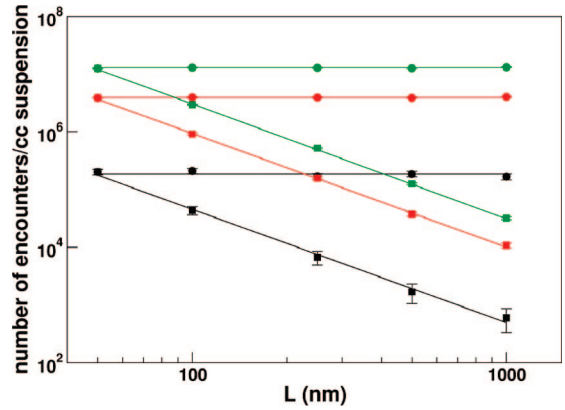

Figure 5. Variation in the number of close encounters/cm^{-3} N_{ce} for Case (I) (circles) and Case (II) (triangles) reported in Table 2. $N_{ce}(r^*)$ is depicted for $r^* = 2b$ (black), $r^* = 3b$ (red), and $r^* = 4b$ (green). Symbols are results from BD simulations. For Case (I), lines represent the average N_{ce}, which is equal to 0.186×10^6, 3.92×10^6, and 12.78×10^6/cm^{-3} for $r^* = 2b$, $3b$, and $4b$, respectively. For Case (II), lines represent best-fits to the expression $N_{ce}(r^*) = kL^{\beta}$, where $k = k(r^*)$ and $\beta \approx 2$.

concentration of nanorods, N_{ce} is independent of L. While this observation may seem rather surprising, it must be noted that a close encounter between nanorods is only a prerequisite for checkmark formation. To consummate a close encounter, the nanorods have to wiggle around until their (102) faces are properly aligned. The speed with which this process occurs is related to the diffusivity of the nanorods, given by eq 2 for example, which clearly favors short nanorods. This fact is made explicit in the kinetic model described in the next section by a length-dependent rate constant.

For Case (II), N_{ce} decreases as the length of the nanorod increases. When the BD simulation data were fit to a power-law expression, $N_{ce} = kL^{\beta}$, we obtained (k, β) = (19.75 ± 0.39, −1.96 ± 0.07), (22.92 ± 0.13, −1.97 ± 0.02), and (24.09 ± 0.08, −1.99 ± 0.01) for $r^* = 2b$, $3b$, and $4b$, respectively. The observed dependence ($\beta \approx -2$) can be explained as follows: for dilute solutions with a uniform distribution of nanorod tips, $N_{ce} \sim c^2$. In Case (II), $c \sim 1/L$. Therefore, $N_{ce} \sim c^2 \sim L^{-2}$.

For both cases, when $r^* = 2b$, the rods appear to align, as mentioned previously, and the average order parameter is 0.58. The orientational correlation decays as r^* increases, and for $r^* = 4b$, the relative conformations are almost isotropic. From Onsager's theory, long-range ordering effects are negligible for $\varphi \ll \varphi_1 = 3.3b/L$, which is certainly valid for all the cases considered in Table 2.[34] Statistically, the order parameters $S(r^*)$ for Case (II) are indistinguishable from those for Case (I) (Figure 6).

d. Kinetics. Since the formation of checkmarks is not modeled explicitly, it is the initial rate of formation of checkmarks that is assumed to be proportional to the number of close encounters, *i.e.*, $r_{CM}(t=0) \propto N_{ce}$. As checkmarks are formed, rods are depleted from the system, and consequently the rate of checkmark forma-

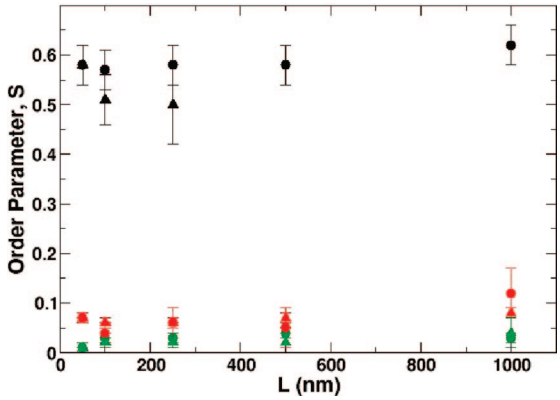

Figure 6. Order parameters $S(r^*)$ for Case (I) (circles) and Case (II) (triangles) reported in Table 2. $S(r^*)$ is depicted for $r^* = 2b$ (black), $r^* = 3b$ (red), and $r^* = 4b$ (green). For $r^* = 2b$, there is strong alignment of the approaching nanorods. However, as r^* increases, the relative orientation disappears and isotropy is recovered.

tion decreases at later times. We considered the kinetics of checkmark formation for the experimental system of short rods (L = 46 nm) in which these superstructures were observed. As shown above, for dilute suspensions, $N_{ce} \sim c^2$. Consider the reaction R + R → CM, where R and CM denote rods and checkmarks, respectively. Assuming second-order kinetics, we have

$$\frac{dc_{CM}}{dt} = r_{CM} = \lambda(L)c(t)^2 \quad (4)$$

where $c_{CM}(t)$ and $c(t)$ are the concentrations of V-assemblies and rods at time t, respectively, and $\lambda(L)$ is a rate constant that depends on the length of the nanorod. From stoichiometry, the concentration of the rods evolves *via*

$$\frac{dc}{dt} = -2\frac{dc_{CM}}{dt} \quad (5)$$

Equations 4 and 5 can be solved using the initial conditions $c_{CM}(t=0) = 0$ and $c(t=0) = c_0$. They yield the following expressions for concentrations:

$$c(t) = \frac{c_0}{1 + 2\lambda(L)tc_0} \quad (6)$$

$$c_{CM}(t) = \frac{\lambda(L)tc_0^2}{1 + 2\lambda(L)tc_0} \quad (7)$$

Experimentally,[35] it appears that, for L = 46 nm, approximately three-fourths of the rods are converted to V-particles over a period of 2 days. If we set $c(t = 2\ \text{days}) = 0.25c_0$ in eq 5, $\lambda(L{=}46\ \text{nm}) = 5.77 \times 10^6\ \text{M}^{-1}\ \text{day}^{-1}$. The concentration profiles are shown in Figure 7. Further, if we assume that N_{ce} remains unchanged over the elemental time interval τ, given by eq 12 in Methods, then the fraction of close encounters that culminate in checkmark formation may be estimated as

$$f_{ce} \approx \frac{r_{CM}(t=0)\tau}{N_{ce}} \quad (8)$$

For L = 46, $f_{ce} \approx 3.08 \times 10^{-5}$. Therefore, the number of close encounters that result in one successful V-assembly on average is $1/f_{ce} \approx 30\,000$. When $c(t=2\ \text{days})/c_0$ is varied between 0.15 and 0.35 (see Figure 7), $1/f_{ce}$ varies between 17 000 and 52 000.

Thus, the formation of V-particles is a rare event. Further, since λ (and f_{ce}) is inversely related to the length of the nanorod, the formation of nanoscale checkmarks for long rods is additionally inhibited.

CONCLUSIONS AND PERSPECTIVE

To study the formation of V-assemblies in nanorod suspensions, we employed BD simulations. We assumed that the incidence of nanoscale checkmark formation was governed by the frequency of proximal interactions between nanorod tips for dilute and semidilute suspensions. On the basis of simulation results, we were able to explain why V-particles were observed for short nanorods, while they were absent for long nanorods.[35] By systematically varying the concentration and the aspect ratio of nanorods, we discovered that concentration set the rate of proximal interactions. When we used only static measurements of dilute nanorod suspensions, the effect of the rod length was found to be relatively unimportant. For dynamic properties or for more concentrated solutions, we expect that the length of the rods would be important. Experimentally, it was observed that V-particles were formed *via* a merger of nanorods of similar lengths. Thus, it is likely that the amount of polydispersity plays a nontrivial role. Directions for future inquiry include elucidating the roles of the dynamics, polydispersity, and energetic interactions between nanorods, with the goal of optimizing synthetic procedures.

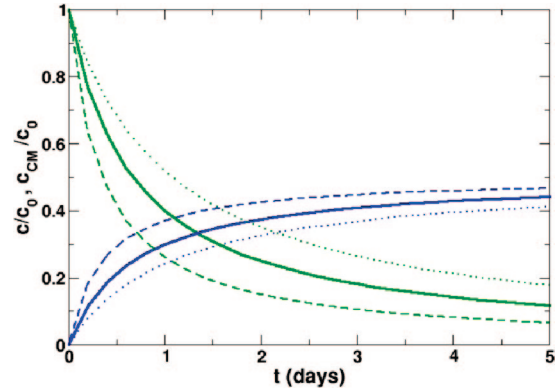

Figure 7. Temporal evolution of the concentration of the rods, c (thick green line), and checkmarks, c_{CM} (thick blue line), using $\lambda = 5.77 \times 10^6\ \text{M}^{-1}\ \text{day}^{-1}$ and $c_0 = 1.3 \times 10^{-7}$ M in the kinetic model. The value of λ was determined by assuming that $c/c_0 = 0.25$ at the end of 2 days. The dashed and dotted lines assume $c/c_0 = 0.15$ and $c/c_0 = 0.35$, respectively, at the end of 2 days.

METHODS

We adopted a sequential BD scheme in which the nanorods were represented as rigid spherocylinders (cylinders with spherical caps, see Figure 4) of length L and diameter b.[36,37] A system of N such rods in a simulation volume V_{sim} were described by their center of mass co-ordinates $\{\mathbf{r}_{cm,1}, \mathbf{r}_{cm,2}, ..., \mathbf{r}_{cm,N}\}$ and orientations $\{\mathbf{\Omega}_1, \mathbf{\Omega}_2, ..., \mathbf{\Omega}_N\}$, where $\mathbf{\Omega}_i$ is a vector of unit magnitude. For symmetrical particles such as spherical colloids, the concentration or number density, ν, determines the average interparticle distance and hence the classification of the solution as dilute, semidilute, or concentrated. To categorize the concentration regime of asymmetric particles such as liquid crystals or nanorods, we require, in addition to the number density, geometrical information such as the length and aspect ratio. A solution of rods is considered to be dilute if $\nu < 1/L^3$ and semidilute if $1/L^3 < \nu < 1/bL^2$.[38] All of the nanorod suspensions considered in this paper were in the dilute or semidilute regime. The concentrated regime is rarely of interest in creating assemblies of nanorods, due to severe transport limitations.

For simplicity, we neglected hydrodynamic and long-range energetic interactions between rods. For charged nanorods, this is equivalent to the assumption that the counterions in the solution effectively screen the charge. Configurations of the system in which rods overlap and thus violate the excluded volume restriction were forbidden. The short-time diffusion of rods was described by three diffusion constants: $D^{\perp}$ and $D^{\parallel}$, perpendicular and parallel to the rod axis, and D^r, a rotational diffusion constant. We used the following analytical expressions for the diffusivities as a function of the aspect ratio $p = L/b$:[39]

$$D^{\perp} = \frac{D_0}{4\pi}\left(\ln p + 0.839 + \frac{0.185}{p} + \frac{0.233}{p^2}\right) \quad (9)$$

$$D^{\parallel} = \frac{D_0}{2\pi}\left(\ln p - 0.207 + \frac{0.980}{p} - \frac{0.133}{p^2}\right) \quad (10)$$

$$D^r = \frac{3D_0}{\pi L^2}\left(\ln p - 0.662 + \frac{0.917}{p} - \frac{0.050}{p^2}\right) \quad (11)$$

where $D_0 = k_B T/\eta L$, where k_B is Boltzmann's constant (1.386×10^{-23} J K^{-1}), T is the absolute temperature, and $\eta = 1$ cP is the viscosity of the solvent. The elemental time scale of a particular nanorod system is

$$\tau = \frac{b^2}{D_0} \quad (12)$$

The number of rods in the simulation box, N, was chosen to be 500 or 1000, and the volume, V_{sim}, was determined from the concentration of the nanorods, c. The system was initialized by generating a random non-overlapping configuration. A rod i was randomly chosen, and a trial move was proposed as follows.[37]

1. The center-of-mass of the ith rod, $\mathbf{r}_{cm,i}$, is decomposed into components parallel and perpendicular to the orientational vector $\mathbf{\Omega}_i$: $\mathbf{r}_{cm,i}^{\parallel} = (\mathbf{\Omega}_i \cdot \mathbf{r}_{cm,i})\mathbf{\Omega}_i$ and $\mathbf{r}_{cm,i}^{\perp} = \mathbf{r}_{cm,i} - \mathbf{r}_{cm,i}^{\parallel}$.
2. Gaussian-distributed random numbers are chosen: $\Delta r^{\parallel}$, with mean zero and variance $2D^{\parallel}\Delta t$, and $\Delta r_1^{\parallel}$ and $\Delta r_2^{\parallel}$, with mean zero and variance $2D^{\parallel}\Delta t$.
3. A trial move is proposed in two steps. First, a trial center-of-mass, $\mathbf{r}'_{cm,i} = \mathbf{r}'^{\parallel}_{cm,i} + \mathbf{r}'^{\perp}_{cm,i}$, is attempted. Here, $\mathbf{r}'^{\parallel}_{cm,i} = \mathbf{r}^{\parallel}_{cm,i} + (\Delta r^{\parallel})\mathbf{\Omega}_i$, and $\mathbf{r}'^{\perp}_{cm,i} = \mathbf{r}^{\perp}_{cm,i} + \Delta r_1^{\perp}\mathbf{e}_{i1} + (\Delta r_2^{\perp})\mathbf{e}_{i2}$, where $\mathbf{e}_{i1}$ and $\mathbf{e}_{i2}$ are two vectors orthogonal to $\mathbf{\Omega}_i$.
4. Next, $\mathbf{\Omega}'_i = \mathbf{\Omega}_i + x_1\mathbf{e}_{i1} + x_2\mathbf{e}_{i2}$ is proposed, where x_1 and x_2 are Gaussian random variables with mean zero and variance $2D^r\Delta t$.
5. If the new configuration $(\mathbf{r}'_{cm,i}, \mathbf{\Omega}'_i)$ is free from overlaps, the move is accepted, and time is incremented by $\Delta t/N$.

A time step $\Delta t = 10^{-4}\tau$ was used, and the simulation was carried out for approximately $t \approx 10^7\tau$. About 1000 snapshots of the simulation system were taken at regular intervals ($\sim 10^4\tau$), and the relative positions and orientations of the nanorods were examined at each snapshot.

Surface Energy of the (100) and (102) Faces. For a Te nanocrystal in the trigonal form, the positions of the atoms and the parameters describing the unit cell were located.[40] The density of atoms on the (100) face is 1.97 Te atoms/nm^2, where the unit cell has $a = b = 0.428$ nm and $c = 0.589$ nm. In a similar geometry, the density of atoms on the (102) face is 1.15 Te atoms/nm^2. According to the Bravais–Friedel–Donnay–Harker theory as well as the Hartman–Perdock theory, the stability of a crystal surface is correlated with the strength of lateral interactions among molecules on a face, which increases as the surface density of molecules on that face increases.[41] Thus, the low-Miller-index face (100), with 1.97 atoms/nm^2, is energetically more stable than the (102) face, and hence the formation of nanocheckmarks is favored.

In the modeling, the short-range energetic interaction between crystal faces of two nanorods approaching each other to form a checkmark is greatly simplified. We assume that the number of nanocheckmarks formed from a nanorod suspension is proportional to the number of "close encounters" between tips of approaching nanorods.

At each simulation snapshot, the number of close encounters is determined according to Figure 4. We define a "sphere of interaction" (SOI) located at the center of both terminal spheres on each spherocylindrical nanorod in the system. We denote by r^* the radius of this SOI. A close encounter is said to have occurred when the volume pervaded by this SOI is penetrated by an approaching nanorod tip, as shown in Figure 4. The distance of closest approach between the terminal spheres on approaching nanorods is denoted by $d^*(i,j)$, where i and j are the indices of the nanorods. Thus, when $d^*(i,j) = b$, nanorods i and j are in physical contact.

In this study, we consider three different values for r^*, namely $2b$, $3b$, and $4b$, where b is the diameter of the nanorod. At each simulation snapshot, we survey all pairs of rods probing for close encounters; *i.e.*, we seek pairs of nanorods (i,j) for which the condition $d^*(i,j) < r^*$ is satisfied. Hence, for a given value of r^*, we can compute the number of close encounters per milliliter of nanorod suspension, $N_{ce}(r^*)$. Since the fraction of close encounters that result in checkmark formation is not known *a priori*, the real-time evolution of the system is not directly simulated. Instead, in section d of the Results and Discussion, the kinetics of the system are considered using a mean-field approach with empirically fitted rate constants. It may be noted that generalized methods to simulate the dynamics of systems consisting of anisotropic particles using molecular simulations have been reported recently in the literature.[42] However, given the inadequate knowledge of the energetic interactions between nanorods, quantitative *ab initio* calculations are not feasible. The presence of residual surfactant stabilizer introduces an additional layer of complexity. Thus, the enormous computational load incurred using methods in which complex shapes are decomposed into elemental spheres is not warranted.

REFERENCES AND NOTES

1. Alivisatos, A. Semiconductor Clusters, Nanocrystals, and Quantum Dots. *Science* **1996**, *271*, 933–937.
2. Xia, Y.; Yang, P.; Sun, Y.; Wu, Y.; Mayers, B.; Gates, B.; Yin, Y.; Kim, F.; Yan, Y. One-Dimensional Nanostructures: Synthesis, Characterization, and Applications. *Adv. Mater.* **2003**, *15*, 353–389.
3. Peng, X.; Manna, L.; Yang, W.; Wickham, J.; Scher, E.; Kadavanich, A.; Alivisatos, A. Shape Control of CdSe Nanocrystals. *Nature* **2000**, *404*, 59–61.
4. Sau, T.; Murphy, C. Seeded High Yield Synthesis of Short Au Nanorods in Aqueous Solution. *Langmuir* **2004**, *20*, 6414–6420.
5. Puntes, V.; Zanchet, D.; Erdonmez, C.; Alivisatos, A. Synthesis of hcp-Co Nanodisks. *J. Am. Chem. Soc.* **2002**, *124*, 12874–12880.
6. Jin, R.; Cao, Y.; Hao, E.; Metraux, G.; Schatz, G.; Mirkin, C. Controlling Anisotropic Nanoparticle Growth Through Plasmon Excitation. *Nature* **2003**, *425*, 487–490.

7. Pastoriza-Santos, I.; Liz-Marzan, L. Synthesis of Silver Nanoprisms in DMF. *Nano Lett.* **2002**, *2*, 903–905.
8. Pinna, N.; Garnweitner, G.; Beato, P.; Niederberger, M.; Antonietti, M. Synthesis of Yttria-Based Crystattine and Lamellar Nanostructures and Their Formation Mechanism. *Small* **2005**, *1*, 112–121.
9. Manna, L.; Scher, E.; Alivisatos, A. Synthesis of Soluble and Processable Rod-, Arrow-, Teardrop-, and Tetrapod-Shaped CdSe Nanocrystals. *J. Am. Chem. Soc.* **2000**, *122*, 12700–12706.
10. Chen, S.; Wang, Z.; Ballato, J.; Foulger, S.; Carroll, D. Monopod, Bipod, Tripod, and Tetrapod Gold Nanocrystals. *J. Am. Chem. Soc.* **2003**, *125*, 16186–16187.
11. Jun, Y.; Lee, S.; Kang, N.; Cheon, J. Controlled Synthesis of Multi-Armed CdS Nanorod Architectures Using Monosurfactant System. *J. Am. Chem. Soc.* **2001**, *123*, 5150–5151.
12. Peng, Z.; Peng, X. Nearly Monodisperse and Shape-Controlled Cdse Nanocrystals via Alternative Routes: Nucleation and Growth. *J. Am. Chem. Soc.* **2002**, *124*, 3343–3353.
13. Manna, L.; Milliron, D. J.; A., M.; Scher, E. C.; Alivisatos, A. P. Controlled Growth of Tetrapod-Branched Inorganic Nanocrystals. *Nature Mater.* **2003**, *2* (6), 382–385.
14. Lee, S.; Jun, Y.; Cho, S.; Cheon, J. Single-Crystalline Star-Shaped Nanocrystals and Their Evolution: Programming the Geometry of Nano-Building Blocks. *J. Am. Chem. Soc.* **2002**, *124*, 11244–11245.
15. Cho, K.-S.; Talapin, D. V.; Gaschler, W.; Murray, C. B. Designing PbSe Nanowires and Nanorings through Oriented Attachment of Nanoparticles. *J. Am. Chem. Soc.* **2005**, *127*, 7140–7147.
16. Cozzoli, P.; Manna, L.; Curri, M.; Kudera, S.; Giannini, C.; Striccoli, M.; Agostiano, A. Shape and Phase Control of Colloidal ZnSe Nanocrystals. *Chem. Mater.* **2005**, *17*, 1296–1306.
17. Jun, Y.; Jung, Y.; Cheon, J. Architectural Control of Magnetic Semiconductor Nanocrystals. *J. Am. Chem. Soc.* **2002**, *124*, 615–619.
18. Jun, Y.; Casula, M.; Sim, J.; Kim, S.; Cheon, J.; Alivisatos, A. Surfactant-Assisted Elimination of a High Energy Facet as a Means of Controlling the Shapes of TiO_2 Nanocrystals. *J. Am. Chem. Soc.* **2003**, *125*, 15981–15985.
19. Polleux, J.; Pinna, N.; Antonietti, M.; Niederberger, M. Ligand-Directed Assembly of Preformed Titania Nanocrystals into Highly Anisotropic Nanostructures. *Adv. Mater.* **2004**, *16*, 436–439.
20. Hao, E.; Bailey, R.; Schatz, G.; Hupp, J.; Li, S. Synthesis and Optical Properties of "Branched" Gold Nanocrystals. *Nano Lett.* **2004**, *4*, 327–330.
21. Sau, T.; Murphy, C. Room Temperature, High-Yield Synthesis of Multiple Shapes of Gold Nanoparticles in Aqueous Solution. *J. Am. Chem. Soc.* **2004**, *126*, 8648–8649.
22. Banfield, J. F.; Welch, S. A.; Zhang, H.; Ebert, T. T.; Penn, R. L. Aggregation-Based Crystal Growth and Microstructure Development in Natural Iron Oxyhydroxide Biomineralization Products. *Science* **2000**, *289*, 751–754.
23. Wang, T.; Reinecke, A.; Coelfen, H. In Situ Investigation of Complex $BaSO_4$ Fiber Generation in the Presence of Sodium Polyacrylate. 2. Crystallization Mechanisms. *Langmuir* **2006**, *22*, 8986–8994.
24. Ribeiro, C.; Lee, E. J. H.; Longo, E.; Leite, E. R. Oriented Attachment Mechanism in Anisotropic Nanocrystals: A "Polymerization" Approach. *Chem. Phys. Chem.* **2006**, *7*, 664–670.
25. Cheng, Y.; Wang, Y.; Chen, D.; Bao, F. Evolution of Single Crystalline Dendrites from Nanoparticles through Oriented Attachment. *J. Phys. Chem. B* **2005**, *109*, 794–798.
26. Tsai, M. H.; Chen, S. Y.; Shen, P. Imperfect Oriented Attachment: Accretion and Defect Generation of Nanosize Rutile Condensates. *Nano Lett.* **2004**, *4*, 1197–1201.
27. Zhang, J.; Wang, Y.; Zheng, J.; Huang, F.; Chen, D.; Lan, Y.; Ren, G.; Lin, Z; Wang, C. Oriented Attachment Kinetics for Ligand Capped Nanocrystals: Coarsening of Thiol-PbS Nanoparticles. *J. Phys. Chem B* **2007**, *111*, 1449–1454.
28. Niederberger, M.; Coelfen, H. Oriented Attachment and Mesocrystals: Non-Classical Crystallization Mechanisms Based on Nanoparticle Assembly. *Phys. Chem. Chem. Phys.* **2006**, *8*, 3271–3287.
29. Tang, Z.; Zhang, Z.; Wang, Y.; Glotzer, S. C.; Kotov, N. A. Self-Assembly of CdTe Nanocrystals into Free-Floating Sheets. *Science* **2006**, *314*, 274–278.
30. Sinyagin, A.; Belov, A.; Tang, Z.; Kotov, N. A. Monte Carlo Computer Simulation of Chain Formation from Nanoparticles. *J. Phys. Chem. B* **2006**, *110*, 7500–7507.
31. Sinyagin, A.; Belov, A.; Kotov, N. A. Monte Carlo Simulation of Linear Aggregate Formation from CdTe Nanoparticles. *Model. Simul. Mater. Sci. Eng.* **2005**, *13*, 389–399.
32. Tang, Z.; Kotov, N. A. One-Dimensional Assemblies of Nanoparticles: Preparation, Properties, and Promise. *Adv. Mater.* **2005**, *17*, 951–962.
33. Tang, Z.; Kotov, N. A.; Giersig, M. Spontaneous Organization of Single CdTe Nanoparticles into Luminescent Nanowires. *Science* **2002**, *297*, 237–240.
34. Tang, Z.; Ozturk, B.; Wang, Y.; Kotov, N. A. Simple Preparation Strategy and One-dimensional Energy Transfer in CdTe Nanoparticle Chains. *J. Phys. Chem.* **2004**, *108*, 6927–6931.
35. Tang, Z.; Wang, Y.; Shanbhag, S.; Giersig, M.; Kotov, N. A. Spontaneous Transformation of CdTe Nanoparticles into Angled Te Nanocrystals: From Particles and Rods to Checkmarks, X-Marks, and Other Unusual Shapes. *J. Am. Chem. Soc.* **2006**, *128*, 6730–6736.
36. Löwen, H. Brownian Dynamics of Hard Spherocylinders. *Phys. Rev. E* **1994**, *50*, 1232–1242.
37. Löwen, H. Anisotropic Self-Diffusion in Colloidal Nematic Phases. *Phys. Rev. E* **1999**, *59*, 1989–1995.
38. Tirado, M. M.; Martinez, C. L.; de la Torre, J. G. Comparison of Theories for the Translational and Rotational Diffusion Coefficients of Rod-like Macromolecules. Application to Short DNA fragments. *J. Chem. Phys.* **1984**, *81*, 2047–2052.
39. Kirchhoff, F.; Binggeli, N.; Galli, G.; Massidda, S. Structural and Bonding Properties of Solid Tellurium from First-Principles Calculations. *Phys. Rev. B* **1994**, *50*, 9063–9071.
40. Myerson, A. S.; Ginde, R. In Crystals, Crystal Growth, and Nucleation. *Handbook of Industrial Crystallization*; Myerson, A. S., Ed.; Butterworth-Heinemann: Boston, MA, 1993; pp 33–63.
41. Zhang, Z.; Glotzer, S. Self-Assembly of Patchy Particles. *Nano Lett.* **2004**, *4*, 1407–1413.
42. Larson, R. *The Structure and Rheology of Complex Fluids*; Oxford University Press: New York, 1999.
43. Doi, M.; Edwards, S. F. *The Theory of Polymer Dynamics*; Clarendon Press: Oxford, 1988.
44. Onsager, L. The Effects of Shapes on the Interaction of Colloidal Particles. *Ann. N.Y. Acad. Sci.* **1949**, *51*, 627–659.